







Article

Photocatalytic Azo Dye Degradation Using Graphite Carbon Nitride Photocatalyst and UV-A Irradiation

Salma A. Al-Zahrani ¹, Mallikarjunagouda B. Patil ^{2,*} , Shridhar N. Mathad ³ , Arun Y. Patil ⁴ , Ahmed Al Otaibi ¹, Najat Masood ¹, Dorsaf Mansour ¹, Anish Khan ⁵ , Vikas Gupta ⁶, Niraj S. Topare ⁷ , Amita Somya ⁸ and Manikandan Ayyar ⁹ 

- ¹ Chemistry Department, Faculty of Science, University of Ha'il, P.O. Box 2440, Ha'il 81451, Saudi Arabia
 - ² Bharat Ratna Prof. CNR Rao Research Centre, P. G. Department of Chemistry, Basaveshwar Science College, Bagalkot 587101, India
 - ³ Department of Engineering Physics, K.L.E Institute of Technology, Hubballi 580030, India
 - ⁴ School of Mechanical Engineering, KLE Technological University, Vidya Nagar, Hubballi 580031, India
 - ⁵ Center of Excellence for Advanced Materials Research, King Abdulaziz University, Jeddah 21589, Saudi Arabia
 - ⁶ Department of Chemistry, Faculty of Science, Motherhood University, Roorkee 247661, India
 - ⁷ School of Chemical Engineering, Dr. Vishwanath Karad MIT World Peace University, Pune 411038, India
 - ⁸ Department of Chemistry, School of Engineering, Presidency University, Bangalore 560064, India
 - ⁹ Department of Chemistry, Bharath Institute of Higher Education and Research (BIHER), Selaiyur, Chennai 600073, India
- * Correspondence: mallupatil04@gmail.com

Abstract: The photocatalytic degradation of Acid Red 26 was examined utilizing a graphitic carbon nitride (g-C₃N₄) catalyst and a UV-A light in this study. We investigated how successfully the photocatalytic approach removed Acid Red 26 from synthetic and actual municipal wastewater. Both aqueous matrices allowed for extremely high clearance rates. Wastewater degraded at a slower rate than the other matrices, this might be ascribed to the wastewater's complicated chemical composition. Using a liquid chromatography-mass spectrometry (LC-MS), the IPs in both synthetic and actual municipal effluent were determined. The photocatalytic degradation mechanisms of Acid Red 26 are hypothesised to comprise oxidation, dealkylation, and methoxy group cleavage based on the observed intermediate products (IPs). Using proven scavengers, we were also able to investigate the role of reactive species in the degradation process and illustrate the significance of h⁺ and O₂[•] in the reaction. *Chlorococcum* sp. and *Dunaliella tertiolecta* microalgae were also utilised to assess the development of ecotoxicity. We observed low toxicity throughout the process when clean water was used as the matrix, with no production of hazardous IPs. In the case of actual municipal wastewater, there was an early rise in toxicity, which scientists believe was caused by the matrix's chemical make-up. To lower the toxicity, a heterogeneous photocatalysis was used, and at the end of the treatment, nearly full detoxification was obtained.

Keywords: photocatalysis; g-C₃N₄; pharmaceuticals; Acid Red 26; reactive species; intermediate products; ecotoxicity



Citation: Al-Zahrani, S.A.; Patil, M.B.; Mathad, S.N.; Patil, A.Y.; Al Otaibi, A.; Masood, N.; Mansour, D.; Khan, A.; Gupta, V.; Topare, N.S.; et al. Photocatalytic Azo Dye Degradation Using Graphite Carbon Nitride Photocatalyst and UV-A Irradiation. *Crystals* **2023**, *13*, 577. <https://doi.org/10.3390/cryst13040577>

Academic Editors: Yu-Chen Liu and Yu-Ze Chen

Received: 27 February 2023

Revised: 21 March 2023

Accepted: 23 March 2023

Published: 28 March 2023



Copyright: © 2023 by the authors. Licensee MDPI, Basel, Switzerland. This article is an open access article distributed under the terms and conditions of the Creative Commons Attribution (CC BY) license (<https://creativecommons.org/licenses/by/4.0/>).

1. Introduction

Aquatic pollution can be derived from chemicals that are released into water bodies through various sources, such as industrial effluents, agricultural runoff, textile industry, hazardous dye waste, and household waste. Chemical pollution can harm aquatic organisms, ecosystems, and human health. Heavy metals, insecticides, medicines, and industrial chemicals are some of the most frequent chemical contaminants encountered in aquatic habitats. Heavy metals, such as mercury, lead, and cadmium are hazardous to aquatic organisms and can build up in the food chain, causing biomagnification. Pesticides, such as herbicides and insecticides, can harm aquatic creatures and disrupt the ecosystem's

balance [1,2]. Pharmaceuticals and personal care items, such as antibiotics and hormones, can also infiltrate bodies of water and impact aquatic organisms, and the long-term implications of low-level exposure to these chemicals remain unknown. Industrial chemicals, such as polychlorinated biphenyls (PCBs) and dioxins are persistent organic pollutants that can linger in the environment for a long time and harm aquatic organisms and human health [3,4]. Chemical pollution prevention and control necessitate effective management and regulation of their use and disposal, the development and use of safer alternatives, and the adoption of treatment technologies to remove these pollutants from bodies of water. Furthermore, public awareness and education are required to decrease inappropriate chemical disposal and encourage responsible environmental practices. Pharmaceutical and textile chemical species enter aquatic systems in amounts ranging from ng/L to µg/L; yet, even at such low levels, they pose a toxicological hazard to live species [5,6].

Azo dyes are synthetic dyes with one or more azo groups ($-N=N-$) as the chromophore, giving them their distinctive colours [6]. They are frequently utilised as colourants in the textile, food, cosmetic, and pharmaceutical industries. Azo dyes are poisonous, and some of them can induce allergic responses or cancer; hence, their usage is strictly regulated in many countries. Azo dyes contribute significantly to water contamination, particularly in underdeveloped nations where laws are low or non-existent [7,8]. Azo dyes can linger in the environment for a long time and are potentially hazardous to aquatic life. Moreover, some azo dyes can degrade into aromatic amines, which are carcinogenic and may endanger human health. To address the issue of azo dye pollution, some governments have imposed restrictions on the use of these dyes and efforts to create safer and more sustainable alternatives are ongoing [9–12].

Acid Red 26 is a synthetic azo dye that is widely used as a colorant in a variety of industries, such as textiles, leather, paper, and food. Acid Red A, Acid Brilliant Scarlet 3R, and C.I. 16150 are some of the alternative names for it. Acid Red 26 is a water-soluble dye that is typically red to reddish-brown in colour but when combined with other dyes, it can generate pink and orange shades [13,14]. Acid Red 26, similar to other azo dyes, has been linked to environmental pollution and probable health hazards, and its usage is restricted in several countries. Acid Red 26 is deemed environmentally harmful due to its ability to produce contamination and harm to aquatic life. When released into bodies of water, it might persist for long periods of time and may not decompose easily, potentially leading to bioaccumulation in the food chain. Furthermore, Acid Red 26 may cause oxygen depletion in bodies of water, which can result in the death of fish and other aquatic species. Many countries control its usage and discharge into the environment in order to prevent or lessen these negative consequences [15–17].

Acid Red 26 can be broken down in a variety of ways, including biological, chemical, and physical processes. Biodegradation, for example, uses microorganisms to break down the colour into less hazardous chemicals. Chemical processes, such as ozonation, advanced oxidation, and reduction can also degrade the dye by destroying the azo link, which is responsible for its colour [18–20]. Adsorption and membrane filtration, for example, can remove colour from the water by trapping it on a surface or selectively permitting it to pass through a membrane. However, the efficiency of these procedures is affected by a number of parameters, including the starting dye concentration, the type of water matrix, and the treatment circumstances [21]. As a result, while selecting a suitable degradation method for Acid Red 26, these variables, as well as the potential environmental impact of the degradation products, should be taken into account.

Acid Red 26 is photodegradable, which means it can be broken down into less dangerous chemicals using light. Acid Red 26 photodegradation usually includes the use of ultraviolet (UV) radiation, which can cleave the azo link, resulting in the production of smaller, less complicated molecules [22]. The starting concentration of the dye, the intensity and wavelength of the light, the presence of additional chemicals in the aqueous matrix, and the kind and concentration of the photocatalyst all influence photodegradation efficiency. While photodegradation can be a successful method for treating Acid Red 26

in water, it should be used with caution due to the potential environmental impact of the degradation products as well as the safety of the UV light and the photocatalysts [23].

A multilayer polymeric semiconductor, g-C₃N₄, is made up of carbon, nitrogen, and hydrogen atoms that are metal-free. Because of its unusual electrical and optical properties, it is a promising material for a variety of applications, such as photocatalysis, energy conversion, and optoelectronics [24]. As g-C₃N₄ absorbs visible light, it is an effective photocatalyst for the breakdown of organic contaminants and the creation of hydrogen from water. Furthermore, g-C₃N₄ is stable, non-toxic, and simple to synthesise using low-cost precursors, making it an appealing alternative to the standard photocatalysts, such as TiO₂ [25]. However, characteristics, such as its shape, crystallinity, and surface qualities, which vary according on the synthesis method utilised, can have an impact on its performance and stability.

Due to its unusual electrical and optical properties, g-C₃N₄ has been widely researched as a catalyst for numerous chemical reactions, including photocatalysis. Additionally, g-C₃N₄ can absorb visible light as a photocatalyst, allowing it to stimulate the breakdown of organic contaminants, the creation of hydrogen from water, and other photo-driven reactions [26,27]. Furthermore, g-C₃N₄ can operate as a heterogeneous catalyst for a variety of chemical transformations under heat circumstances, including alcohol oxidation, amination, and coupling reactions. Modifying the surface characteristics of g-C₃N₄ as a catalyst, doping with other elements, or creating composite materials with other catalysts or supports can all improve its efficacy as a catalyst. However, issues, such as a limited catalytic activity, poor stability, and difficulty in large-scale synthesis remain, necessitating additional study and development [28–31].

In addition, g-C₃N₄ has demonstrated considerable promise as a photocatalyst in a variety of environmental and energy applications [28–32]. As a photocatalyst, g-C₃N₄ may absorb visible light, allowing it to enhance photo-driven processes, such as organic pollutant degradation, hydrogen synthesis from water, and carbon dioxide reduction. The use of g-C₃N₄ as a photocatalyst has a number of advantages, including non-toxicity, low cost, and stability in ambient circumstances [33]. Furthermore, by altering its structure, such as doping with other elements, its bandgap energy can be altered, which can improve its photocatalytic performance [34]. However, the photocatalytic efficacy of g-C₃N₄ can be influenced by parameters, such as crystallinity, shape, and surface characteristics, which can vary depending on the synthesis process used [35]. Researchers have also investigated the formation of g-C₃N₄-based composite materials with other photocatalysts or supports to improve their photocatalytic efficiency. Overall, the use of g-C₃N₄ as a photocatalyst is a promising field of research that has the potential to help develop sustainable and clean energy systems [35].

When it comes to photodegradation of reactive azo dyes, ultraviolet (UV) radiation outperforms visible light in several ways. As UV radiation has more energy than visible light, it can more easily break the chemical bonds between the dye molecules and release the dye. This improves its ability to decompose the colour into less hazardous chemicals. The fact that UV light is absorbed by the dye molecules' chromophoric groups promotes photodegradation of reactive azo dyes. Additionally, because of its selectivity, the dye may be degraded faster and with less energy lost due to unintended reactions. UV light can quickly destroy reactive azo dyes, usually within minutes or hours, depending on the strength of the radiation and the dye's properties. Its rapid breakdown may reduce the treatment's duration and power requirements, making it less expensive [36]. There are no waste products: As far as we know, UV photodegradation does not produce any toxic by-products that could endanger wildlife or humans. This guarantees that the method can be used without fear of polluting or contaminating the environment. To sum up, UV radiation's benefits make it a viable approach for the photodegradation of reactive azo dyes, especially in industrial and wastewater treatment applications where vast quantities of dye-contaminated water need to be treated rapidly and effectively [37,38].

However, the ecotoxicity assessment of the photocatalytic treatment, identification of the intermediate products (IPs), and use of g-C₃N₄ catalysts for AR-26 azo dye degradation under different matrix environments have yet to be explored. The major goal of this study was to see if a g-C₃N₄ catalyst could be utilised to photocatalyze the degradation of the AR-26 azo dye in the presence of UV-A irradiation, and if so, what IPs were formed. The toxicity was further assessed using the microalgae *Chlorococcum* sp. and *Dunaliella tertiolecta*. Furthermore, the function of the reactive species in degradation was assessed.

2. Materials and Methods

2.1. Chemicals and Reagents

We obtained our azo dye Acid Red 26 from Loba Chemie (Mumbai, India). The photocatalyst in this case was graphitic carbon nitride (g-C₃N₄) [8,32]. The physical properties of the graphite carbon nitride measured in the laboratory are tabulated in Table 1; these were thought to be important for this study. As for the solvents, Fisher Chemical provided HPLC-grade acetonitrile, isopropanol, methanol, and water (Mumbai, India). p-benzoquinone, formic acid, Cyanobacteria BG-11 were provided by Freshwater Solution, and Guillard's (F/2) Marine Water Enrichment Solution was obtained from Sigma-Aldrich (Bangalore, India). We used purified water and treated wastewater matrices. Table 2 lists some of the properties of the wastewater measured in the laboratory. The remaining reagents were all of analytical quality. Throughout the experiment, double-distilled water was used.

Table 1. Physical properties of graphite carbon nitride.

Sl. No.	Property	Value
1	BET Surface area	36 m ² /g
2	particle size	30 nm
3	Energy gap (E _g)	~2.84 eV

Table 2. Treated wastewater characteristics.

Sl. No.	Property	Value
1	pH	7.5 ± 0.3
2	Conductivity	310.72 ± 10 µS/cm
3	Total suspended solids	1.88 ± 0.31 mg/L
4	COD	18.1 ± 1.89 mg/L
5	PO ₄ ^{3−}	3.87 ± 0.05 mg/L
6	SO ₄ ^{2−}	32.4 ± 1.44 mg/L
7	NO ₃ [−]	25.3 ± 0.77 mg/L

2.2. Photocatalytic Experiments

Experiments on photocatalysis were carried out utilising a setup that includes four Philips black light tubes (with a peak emission of 356 nm). The photoreactor was a 250 mL cylindrical quartz cell. The 100 mL of reference sample and pollutant samples were taken for the experiment. A typical experiment included the following parameters: [AR-24]₀ = 1 mg/L; [g-C₃N₄] = 300 mg/L. To reach the adsorption equilibrium, the suspensions were maintained in the dark for 45 min prior to initiating the radiation. Under these conditions, the actinometer potassium ferrioxalate was utilised on a regular basis to determine that the photon flux (I₀) entering the solution was 1.1 ± 0.03 µEinstein/s [39,40]. The catalyst particles were collected and discarded using a PVDF membrane filter with 0.22 µm pore size (Millex-GV).

2.3. Scavenging Experiments

Scavengers, similar to isopropanol, p-benzoquinone, and methanol are frequently used to identify reactive oxygen species (ROS) in chemical reactions. The ability of these scavengers to quench or scavenge specific ROS can be evaluated by adding them at specific concentrations, and the contribution of each ROS to the degradation process can be determined. In this case, isopropanol is frequently used to scavenge hydroxyl radicals (HO^\bullet), p-benzoquinone for superoxide anion radicals ($\text{O}_2^{\bullet-}$), and methanol for positive holes (h^+). We can determine the relative contribution of each ROS to the degradation by adding these scavengers at specified concentrations and evaluating the degradation process. The contribution of hydroxyl radicals (HO^\bullet), superoxide anion radicals ($\text{O}_2^{\bullet-}$), and positive holes (h^+) in the decomposition processes was explored by using scavengers, such as isopropanol (0.1 M), p-benzoquinone (0.2 mM), and methanol (0.1 M) [41].

2.4. Analytical Methods

Using a Dionex (Make: Thermo Scientific, Waltham, MA, USA, Model: Ultimate 3000 UHPLC) equipped with an AcclaimTM RSLC 120 C18 capillary column, the amount of Acid Red 26 in the sample was computed (Thermo Scientific, Waltham, MA, USA). The mobile phase consisted of 0.15 mL/min of acetonitrile (80%) and distilled water containing 0.1% formic acid (20%) at a constant flow rate. This detection was conducted at the maximum pollutant λ_{max} concentration.

2.5. HPLC/MS Analysis

The HPLC-MS is a useful analytical tool for analysing photodegradation products in a variety of matrices, including environmental samples, polymers, pharmaceuticals, and food. Photodegradation is the breakdown of molecules under the influence of light, which can result in the formation of a variety of photoproducts. The HPLC-MS technique is used to identify and quantify photodegradation products as well as to assess the degree of degradation. The technique involves using high-performance liquid chromatography (HPLC) to separate the photodegradation products and then using mass spectrometry to detect the individual components (MS). Using an ion trap mass spectrometer (Bruker, Billerica, MA, USA) attached to an HPLC/MS system (Cecil Instruments Limited, Bath, BA2 9AP, London, UK) allowed us to identify the presence of IPs in the samples.

2.6. Algal Biotest

The bioassays were carried out on *Chlorococcum* sp. (strain SAG 22.83) and *Dunaliella tertiolecta* (CCAP19/6B) under sterile conditions and constant lighting according to the OECD 201 protocol [35] (4300 lux). Freshwater (BG-11) and saltwater (F/2) algae were cultured. The tests began with a consistent supply of logarithmic growth cells (1×10^4 cells/mL), which was maintained by transferring stock algal cultures to conical flasks using the appropriate media (final volume 100 mL). At each stage, samples were collected and examined in duplicate cultures for 96 h while being constantly stirred. The cells were counted using a Neubauer haemocytometer. The growth rate (μ) and the percentage of the growth rate inhibition were then computed. The data are presented in the form of a mean standard deviation.

2.7. UV-Visible Spectrophotometric Analysis

The photodegradation of the dye can be monitored by measuring changes in the absorbance spectrum of the solution over time. Typically, the absorbance of the dye at a specific wavelength is measured at regular intervals, and the percentage degradation of the dye is calculated based on the decrease in absorbance over time. The UV-Visible spectroscopy is a useful technique for a photodegradation analysis of dyes because it is a non-destructive, non-invasive, and highly sensitive method. Additionally, it is relatively easy to perform, and the equipment required is widely available in many laboratories [42].

The reaction mixture was pipetted out and analysed for composition at regular intervals. To track the reaction development, spectrophotometric (Make: Systronics, Model: 118, Mumbai, India) measurements were obtained at the maximum of the reaction mixture using a spectrometric quartz cell (1 cm in path length). As the reaction develops, the absorbance of the reaction mixture decreases. According to the Beer–Lambert rule, a dye’s absorbance is proportional to its concentration.

$$A = ecl$$

where e is the molar absorption coefficient and l is the absorption cell thickness. Given that the molar absorption coefficient (e) and cell thickness (l) remain constant, there is a linear relationship between the concentration of the dye in the reaction mixture and its absorbance over time. The initial rate technique was used to investigate the kinetics of these processes. The plane mirror technique was used to establish the initial reaction rate $(da/dt)_i$ of each set, which entailed constructing a graph between the absorbance values at matching periods and measuring the slope of the curve.

3. Results and Discussion

3.1. XRD

The g-C₃N₄ particles’, as prepared XRD patterns, are displayed in Figure 1. The g-C₃N₄ diffraction peaks are located at 8.1° and 25.5° for the (100) and (002) planes, respectively, as shown in Figure 1. These two peaks are most likely caused by an interplanar gap between the tri-s-triazine unit and the conjugated aromatic system [42,43]. This enabled the synthesis of g-C₃N₄.

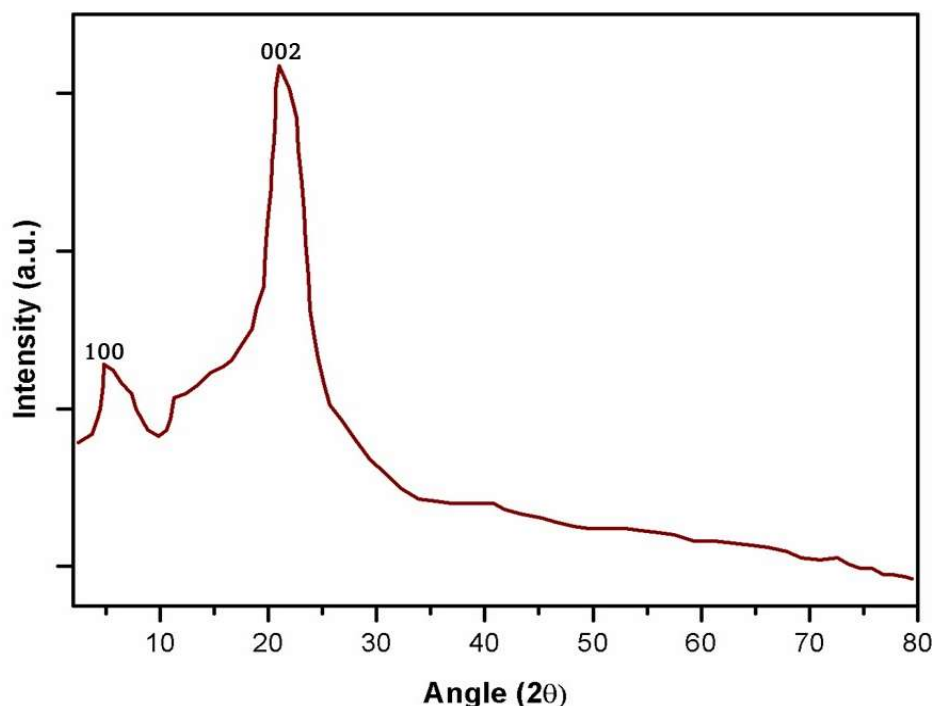


Figure 1. X-ray diffraction (XRD) patterns of the graphitic carbon nitride (g-C₃N₄).

3.2. TGA

The findings of a TGA examination of the behaviour of g-weight-change C₃N₄ are provided. The heating rate was 5 °C/min, and the temperature ranged from room temperature to 700 °C. The first peak, induced by water and solvent desorption, developed between 100 and 300 degrees Celsius, as shown in Figure 2. The second peak temperature of 400 to 600 degrees Celsius is produced by the combustion of g-C₃N₄ in air. Even at the optimal

testing temperature of 300 °C, the test results demonstrate that g-C₃N₄ was not broken down.

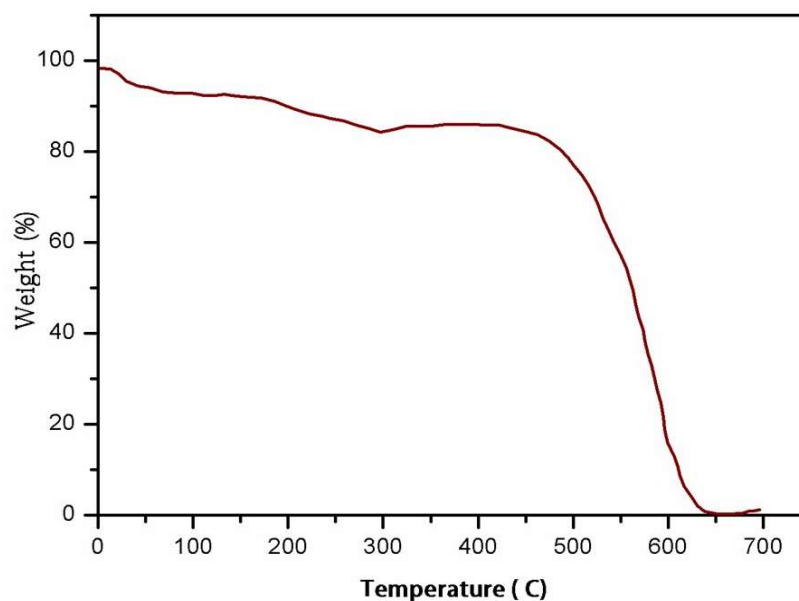


Figure 2. Thermogravimetry–differential thermal analysis (TGA) profiles of g-C₃N₄.

3.3. Photocatalytic Degradation Kinetics

Photodegradation, or the breakdown of organic molecules using ultraviolet (UV) radiation, is a common approach for dealing with environmental toxins present in water and air. The UV radiation photochemically reacts with the organic molecules, which may lessen their toxicity by reducing their molecular weight. UV (ultraviolet) light is classified into three wavelength ranges: UV-A (320–400 nm), UV-B (280–320 nm), and UV-C (280 nm) (100–280 nm).

UV-A (ultraviolet-A) light is frequently used to produce photodeterioration for a variety of reasons, including: (a) Accessibility: The most prevalent and readily available type of UV radiation from the sun is ultraviolet A (UV-A). Artificial UV sources, such as UV lights, can easily generate it, (b) UV-A has a stronger penetrating potential than the other UV spectrum regions. Deeper penetration into the water or treated item results in a more efficient photodegradation, (c) UV-A is less harmful to humans and the environment than UV-B and UV-C. UV-C, for example, it is ideal for photodegradation but can harm humans by causing skin and eye damage and polluting the environment, (d) As UV-A requires less energy to produce than UV-B and UV-C, it is more cost-effective for industrial-scale photodegradation, (e) UV-A light is a promising option for photodegradation applications due to its accessibility, penetrating power, low environmental impact, and efficient energy use.

Prior to researching the AR-26 photocatalytic degradation, the initial control examinations (adsorption and UV photolysis) were performed in pure water, the findings are shown in Figure 3. The equilibrium was attained after 30 min, and approximately 14% of the AR-26 was eliminated utilising the adsorption studies. The UV-Vis spectra of AR-26 explains the little drop (~6.3%) in AR-26 caused by photolysis under UV-A light. Direct photolysis under UV-A light was not expected under the conditions utilised since the AR-26 does not absorb at 356 nm (the maximum emission wavelength of the chosen irradiation source).

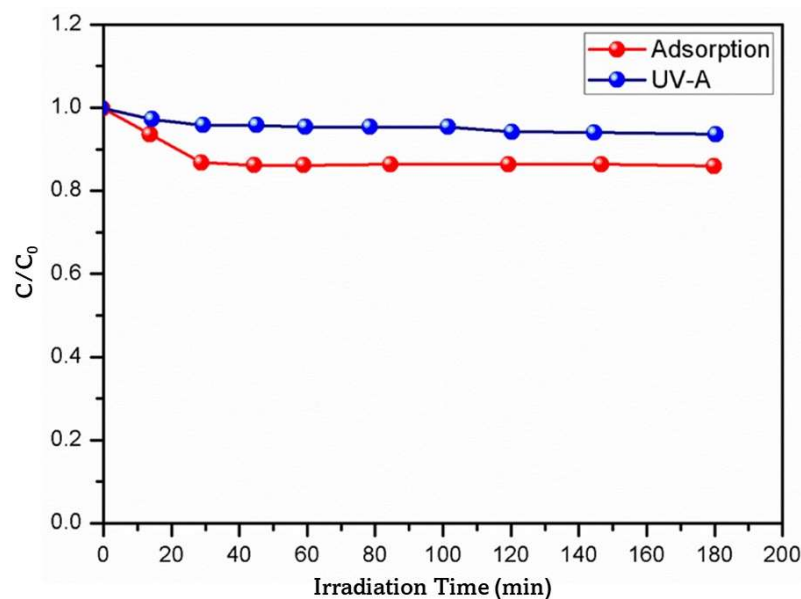


Figure 3. Photolysis of AR-26 via adsorption and photolysis using UV-A light in pure water ($[AR-26]_0 = 1 \text{ mg/L}$; $[g-C_3N_4] = 300 \text{ mg/L}$).

The findings of the examination of the g-photocatalytic C_3N_4 activity under a UV-A source in both the pure water and treated wastewater are shown in Figure 4. According to the photocatalytic analysis, when the $g-C_3N_4$ is exposed to light with an energy greater than its bandgap ($\sim 2.844 \text{ eV}$), it becomes activated and creates a photo-induced electron-hole pair ($e^- - h^+$) and other reactive species that are responsible for the destruction of the AR-26. The AR-26 degradation kinetics (rate constants, half-lives, and correlation coefficients) are presented in both matrices and are shown in Table 3. The experimental data was fitted using pseudo-first order reaction kinetics. Both matrices achieved significant reductions (Figure 4). The degrading percentages in pure water were around 86.0 after 60 min, while in treated wastewater they were around 68.0 after 180 min [8,13].

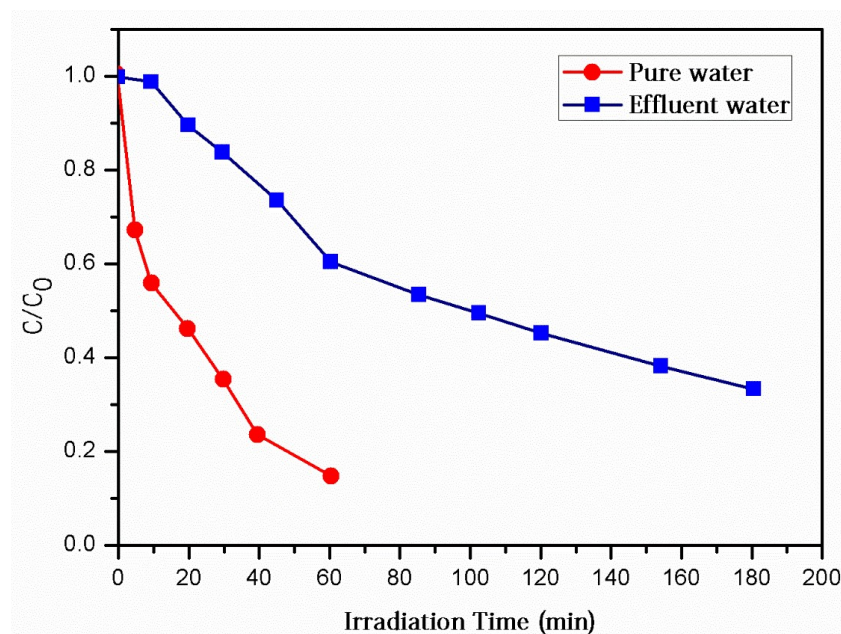


Figure 4. Degradation of AR-26 via photocatalysis in pure water and effluent water exposed to UV-A light ($[AR-26]_0 = 1 \text{ mg/L}$; $[g-C_3N_4] = 300 \text{ mg/L}$).

Table 3. (AR-26) photocatalytic degradation in pure water and effluent water: various kinetic parameters (rate constants, correlation coefficients (R^2), half-lives ($t_{1/2}$)).

Matrix	$K \times 10^{-2} \text{ (min}^{-1}\text{)}$	$t_{1/2} \text{ (min)}$	R^2
Pure water	3.11	23.12	0.9524
Effluent water	0.72	99.12	0.9821

Pure water showed a faster rate of deterioration than the effluent water. Specifically, the half-life of the AR-26 in pure water was determined to be $t_{1/2} = 22.84$ min minutes at a rate constant of $k = 3.05 \times 10^{-2}/\text{min}$. A significantly slower depreciation of the AR-26 was seen in the effluent water ($k = 0.7 \times 10^{-2}/\text{min}$ and $t_{1/2} = 98.91$ min).

This pattern demonstrates the significant influence of the water matrix composition on the photocatalytic performance. The organic and inorganic components (e.g., Cl^{-1} , HCO_3^{-1} , NO_3^{-1} , SO_4^{-2}) that coexist in effluent water may influence the photocatalytic activity, primarily as reactive species scavengers [44,45]. The adsorption of the effluent water components onto the surface of a catalyst can change the surface charges and reduce the number of active sites [46]. However, the metal ions in the effluent water may have a negative impact on the photocatalytic efficiency. Cu^{+2} , Zn^{+2} , Fe^{+3} , and Al^{+3} were found to have an inhibiting effect on the photocatalytic performance under the experimental conditions studied. The results are tabulated in Figure 5. The metal ions may influence the photocatalytic degradation by (i) preventing O_2 from being reduced by photogenerated conduction electrons; hence, inhibiting the generation of reactive oxygen species [47], and (ii) altering the pollutant adsorption. The degradation of the AR-26 was examined using effluent water as a matrix, and the effect of pH was measured under similar conditions and the results were plotted in Figure 6. The AR-26 was most successfully removed at a neutral pH (about 7.8). The used catalyst was discovered to have a pH-PZC of roughly 5.0. The catalyst surface is negatively charged if the value is less than or equal to this threshold; otherwise, it is positively charged. The AR-26 (pK_a 9.46) molecules are largely protonated at pH 7.8 in a similar way. Under the testing conditions, the highest removal is accomplished due to the electrostatic attractions between the AR-26 and the negatively charged catalyst's surface. At pH = 4, however, the breakdown is significantly hindered due to the electrostatic repulsion between the positively charged catalyst molecules and the negatively charged AR-26 molecules. Under pH = 10, some electrostatic repulsion between the negatively charged catalysts and the partly negative charged AR-26 molecules might be assumed to verify the minor reduction in the degradation observed.

3.4. Role of Reactive Species to the Degradation Mechanism

To determine the presence of HO^\bullet , h^+ , and O_2^\bullet , isopropanol (IPA), methanol (MeOH), and p-benzoquinone (p-Bqn) were used. The scavengers were selected because of their consistently high reaction rates with their target species. As it has a high-rate constant reaction with the radical, equal to $2.1 \times 10^9 \text{ L/mol/s}$, the IPA is recognized to be an excellent HO^\bullet scavenger [23,24]. MeOH reacts with HO^\bullet at a rate of $1.1 \times 10^9 \text{ L/mol/s}$ [20,25], making it efficient against both HO^\bullet and h^+ . The rate constant for quenching $\text{O}_2^{\bullet-1}$ by para-benzoquinone (p-Bqn) is $1.8 \times 10^9 \text{ L/mol/s}$ [20]. The pseudo-first order rate constants and the degradation profiles in the presence of the scavengers are shown in Table 4 and Figure 7, respectively.

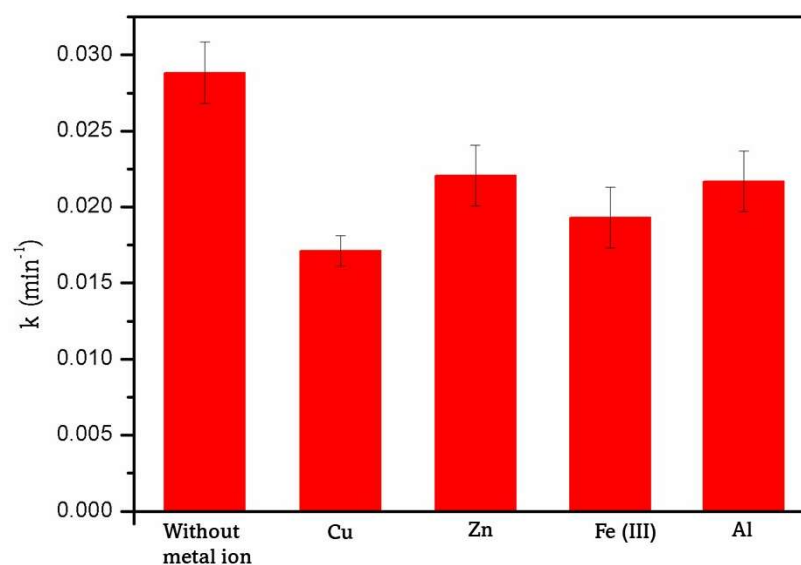


Figure 5. A comparison study of the photocatalytic degradation of AR-26 in pure water ($[AR-26]_0 = 1 \text{ mg/L}$, $[metal\ ion]_0 = 10 \text{ mg/L}$, $[g-C_3N_4] = 300 \text{ mg/L}$) with and without metal ions.

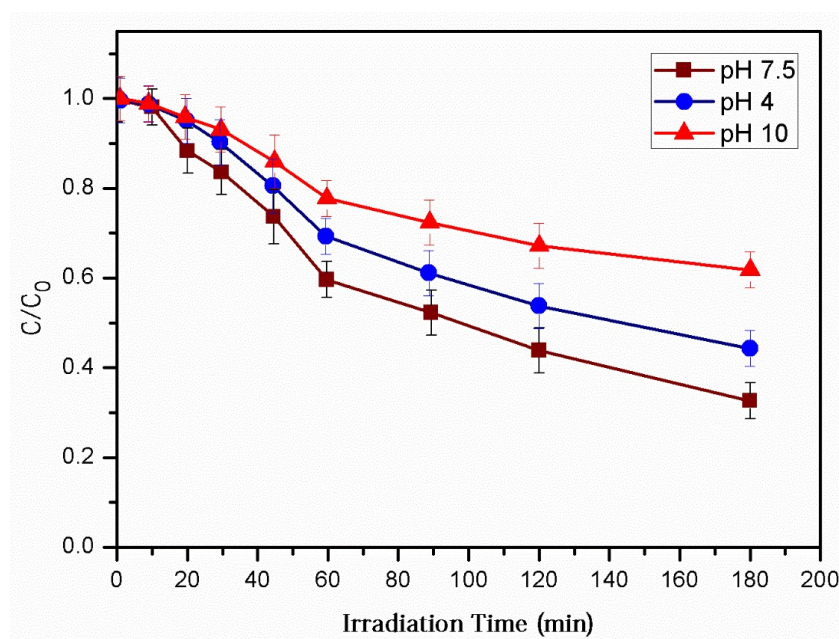


Figure 6. pH-dependent effects on photocatalytic degradation of AR-26 in effluent water ($[AR-26]_0 = 1 \text{ mg/L}$, $[g-C_3N_4] = 300 \text{ mg/L}$).

Table 4. Photocatalytic degradation of AR-26 in the presence of scavengers: kinetic parameters (rate constants, correlation coefficients (R^2), and percentages of inhibition ($\% \Delta k$)).

Scavenger	$K \times 10^{-2} \text{ (min}^{-1}\text{)}$	R^2	$\% \Delta k$
Without Scavenger	3.11	0.9524	-
IPS	1.77	0.9821	42.3
Methanol	0.24	0.9391	92.9
p-Bpo	0.83	0.9813	74.1

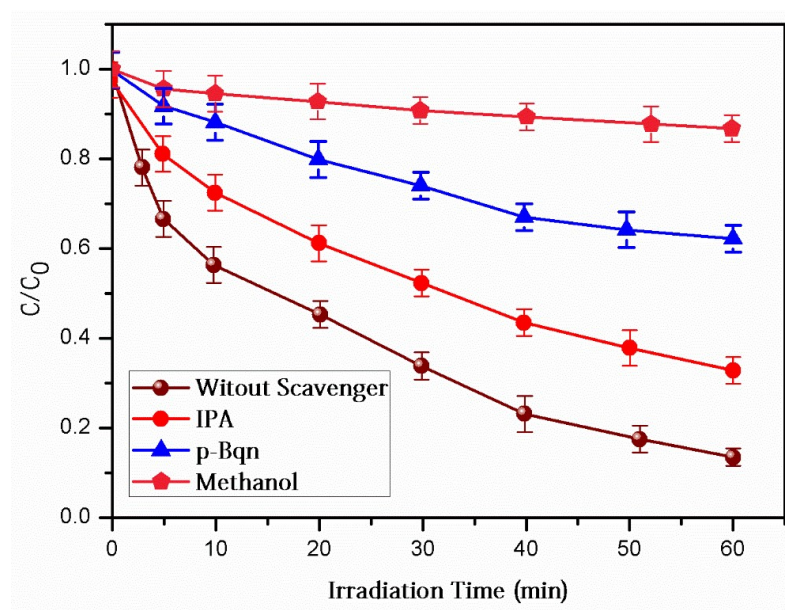
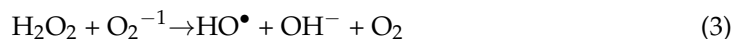


Figure 7. In the presence of scavengers, photocatalytic degradation of AR-26 was observed ($[AR-26]_0 = 1 \text{ mg/L}$; $[g-C_3N_4] = 300 \text{ mg/L}$; $[IPA] = 0.1 \text{ M}$; $[MeOH] = 0.1 \text{ M}$; $[p-Bqn] = 0.2 \text{ mM}$, matrix: pure water).

Graphitic carbon nitride ($g-C_3N_4$) has a conduction band edge potential in the range of -1.1 to -0.6 V relative to a conventional hydrogen electrode at room temperature. In the conduction band of $g-C_3N_4$, 0.94 eV of energy is needed to create superoxide radicals ($O_2^{\bullet-}$) from O_2 . This is roughly equivalent to a potential of -0.4 V with respect to the normalised hydrogen electrode. In light of the above, it may be concluded that g -conduction C_3N_4 's band edge potential is certainly high enough to generate superoxide radicals from O_2 .

MeOH achieved the largest decrease (94.2%) because it can neutralize both HO^{\bullet} and h^+ . The fact that IPA only generated a 42.7% inhibition highlights both the limited contribution of HO^{\bullet} and the major participation of h^+ . This is consistent with the literature's findings: Because the VB edges of $g-C_3N_4$ catalysts are still less positive than the OH/HO^{\bullet} redox potential (1.99 eV vs. NHE) [48], the formation of HO^{\bullet} via direct water or OH oxidation by holes is discouraged during activation. The experiments in acetonitrile verified the significance of h^+ (data not shown). The inhibition rate increased to 73.8% when p-Bqn was added. The superoxide anions were found to directly oxidize organic pollutants. The reactions [49] that additionally comprise $O_2-O_2^{\bullet-1}$ and result in the formation of HO^{\bullet} are as follows:



Our results support those of a recent study [46], which used $g-C_3N_4$ -based catalysts in the photocatalytic destruction of refractory pollutants. The key species reported to be involved in this process were h^+ and $O_2^{\bullet-}$. The proposed photocatalytic mechanism, as observed in the prior work, is based on the formation of electron-hole pairs in the valence and conduction bands of $g-C_3N_4$. The e^- on the CB may convert O_2 to $O_2^{\bullet-}$, while the holes (h^+) in the VB actively contribute to the degrading process in $g-C_3N_4$. $O_2^{\bullet-1}$.

3.5. Photocatalytic Degradation Mechanism

Using mass spectrometry and interpreting mass spectra collected in positive ionisation mode, we were able to establish which IPs are formed during the early stages of the photocatalytic reactions in both pure water and wastewater. Three IPs were identified structurally in both matrices using molecular and fragment ions as shown in Table 5.

Table 5. The detected IPs' in mass (in terms of $[M + H]^+$) and chemical formulae.

IP's	$[M + H]^+$	Molecular Formula
AMI	435	$C_{18}H_{12}O_7N_2S_2$
AMI-1	330	$C_{10}H_4O_7N_2S_2$
AMI-2	270	$C_{10}H_7O_5N_2S$
AMI-3	241	$C_{10}H_8O_5S$
AMI-4	170	$C_8H_8O_4$
AMI-5	152	$C_8H_8O_3$

Figure 6 depicts one of three potential paths. In the first, the methoxy group of AR-26 is removed, resulting in AMI1. In addition to our findings, Skibiski et al., 2011 [50,51] discovered this IP during the photodegradation of the studied pharmaceutical. AR-26 was discovered through the photocatalytic treatment of an effluent mixture containing it. The first step in the dealkylation pathway, the alternative metabolic route, is cleavage of the ethyl group attached to the N atom. Through the third pathway, an oxygen transfer mechanism results in the formation of a signature N-oxide IP. N-oxide was discovered to be a characteristic IP while treating AR-26 using photolysis [51] and heterogeneous photocatalysis. The absence of hydroxylated IPs support the reports that HO^\bullet plays only a minor role in the degradation mechanism. Prior research on the photocatalytic degradation of AR-26 containing effluent mixtures [52] is consistent with the proposed degradation pathways. The possible route of Acid Red 26's decomposition is shown in Figure 8.

The formation of the IP was also tracked during the photocatalytic process. According to Figure 9, the IPs in pure water (Figure 9a) and effluent water (Figure 9b) reached their maximal area in 20 and 60 min, respectively. The space occupied by the three IPs in both matrices shrunk substantially after that. Before full mineralization, the rings can be split, permitting the generation of IPs with low molecular weight. After extensive usage of heterogeneous photocatalysis, formic and acetic acid, both with low molecular weights, were identified.

3.6. Ecotoxicity Evolution

The toxicity to microalgae was measured over time in both saltwater and freshwater environments (Figures 10 and 11). As shown, pure water showed little toxicity at 0 min into the process (Figures 10a and 11a). In comparison, after 72 h of contact with an untreated AR-26 solution in effluent water (0 min), the growth rates of both microalgae were inhibited by nearly 25%. (Figures 10b and 11b). This matrix's composition, which may be toxic for the exposed microalgae, may explain the significant growth inhibition rates found in effluent water. Toxicity tests on an early wastewater sample verified this, with an inhibition rate of 18.1%. The obtained results were in accordance with the previously reported literature and found essentially the same patterns [44,53]. It was discovered that the earliest stages of the photocatalytic treatment only slightly increased the toxicity in both matrices. There is a connection between the emergence of these IPs and the observed increase. Notably, in pure water and effluent water, the IPs developed most strongly at 20 and 60 min, respectively, implying that these intervals are critical for growth inhibition. The photocatalytic degradation of numerous pollutants in aqueous matrices by various AOPs has also been reported to have increased the toxicity in the early stages, which is consistent with our findings [53]. However, the Ips play a modest role in the overall toxicity.

In all cases, the percentage of inhibition was significantly reduced after photocatalytic treatment. This clearly demonstrates that g-C₃N₄-based heterogeneous photocatalysis can occur without the generation of dangerous IPs. It also efficiently reduces the harmful impacts of municipal wastewater.

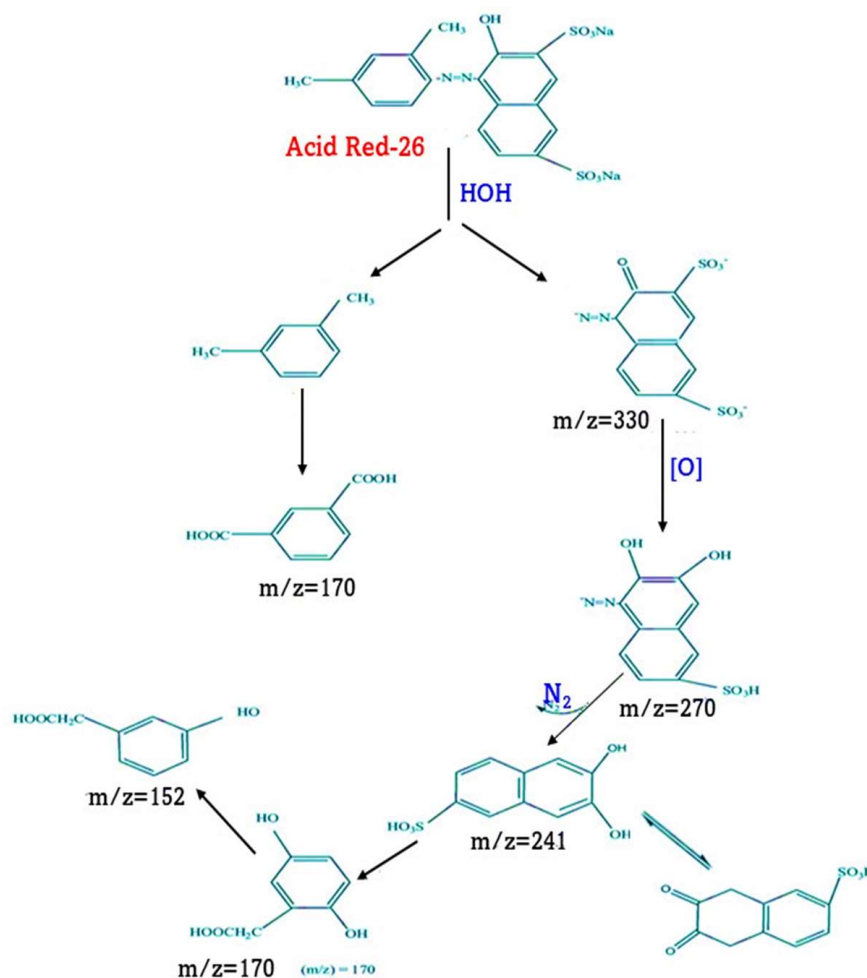


Figure 8. A possible route of Acid Red 26's decomposition.

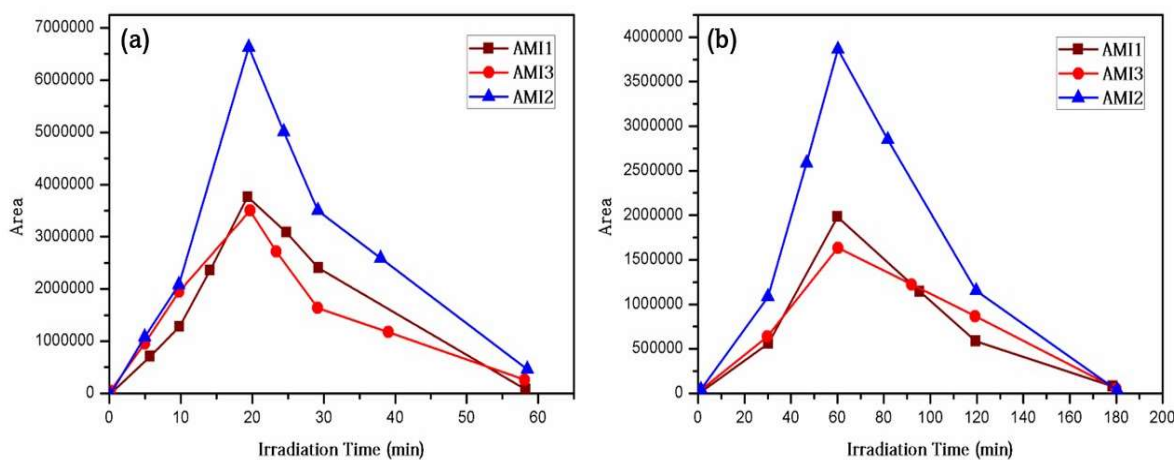


Figure 9. A comparison of the IP generation patterns in (a) pure water and (b) effluent water during the photocatalytic degradation of AR-26 ([AR-26]₀ = 1 mg/L; [g-C₃N₄] = 300 mg/L).

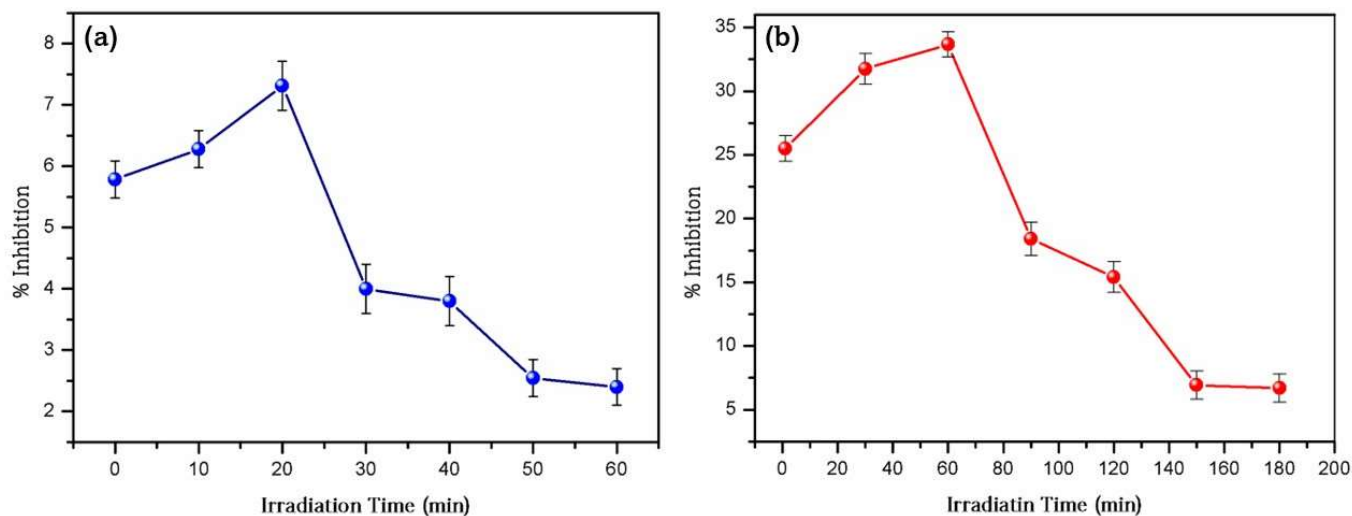


Figure 10. Toxicity changes during photocatalysis with AR-26 in (a) pure water and (b) effluent water at $[AR-26]_0 = 1 \text{ mg/L}$ and 300 mg/L , respectively).

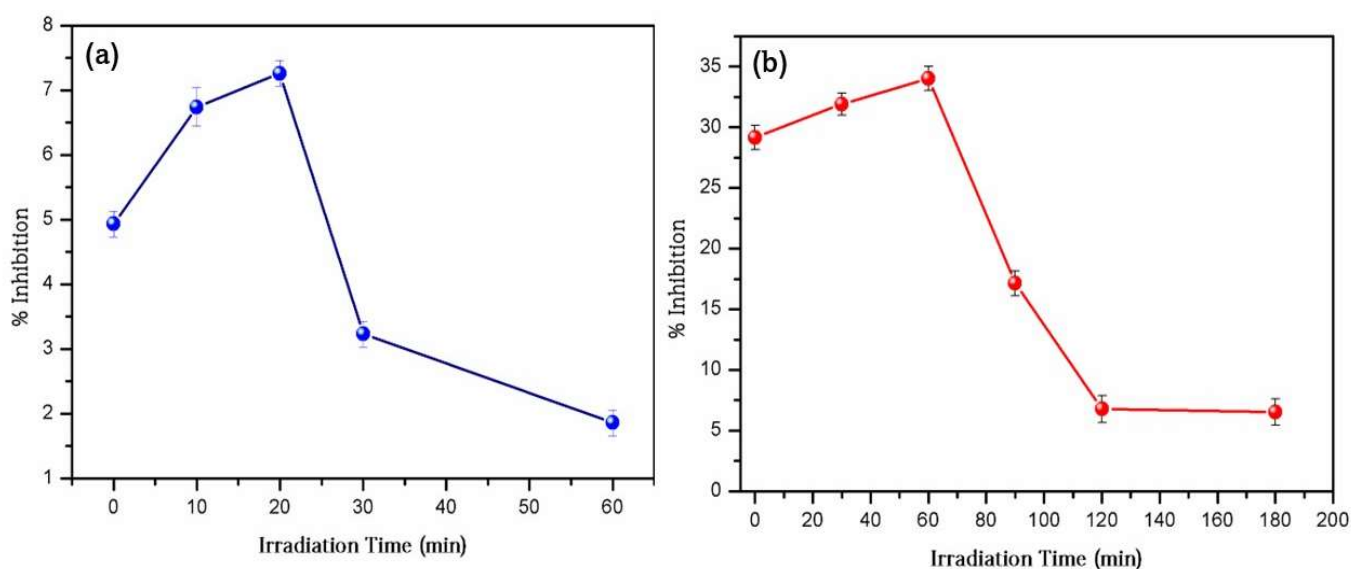


Figure 11. Toxicological changes in *Dunaliella tertiolecta* during photocatalysis in (a) pure water and (b) conventional water ($[AR-26]_0 = 1 \text{ mg/L}$; $[g-C_3N_4] = 300 \text{ mg/L}$).

3.7. A Catalytic Investigation into the Oxidation of Azo Dyes

The oxidation of azo dyes i.e., AR-26 was examined using $g-C_3N_4$ to determine the catalytic efficacy of $g-C_3N_4$. The UV-A irradiation on the samples was carried out for a period of 45 min. The decomposition of the azo dyes was tracked using a kinetic spectrophotometric analysis. Figure 12 depicts the UV-vis spectrum of the AR-26 breakdown. AR-26 has a maximum absorption wavelength of 510 nm. New bands at 245 and 273 nm indicate dye degradation in this case as well.

3.8. Recyclability and Photostability

Five photocatalysis cycles were carried out to test the photocatalyst's reusability. Figure 13 depicts many samples of the photographs. Figure 13 shows that the efficiency of the photocatalysis remains constant after five rounds. Furthermore, as shown in Figure 13, the XRD measurements performed after the photocatalytic phenomena show that the

crystalline structure of $g\text{-C}_3\text{N}_4$ has not altered in comparison to before the photocatalytic process was carried out.

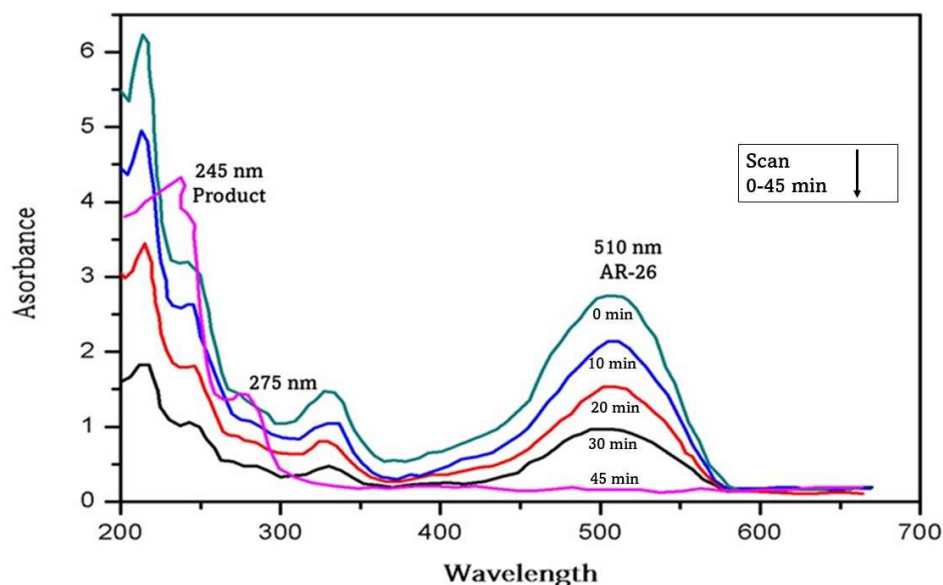


Figure 12. UV-vis spectra showing the degradation of Acid Red-26.

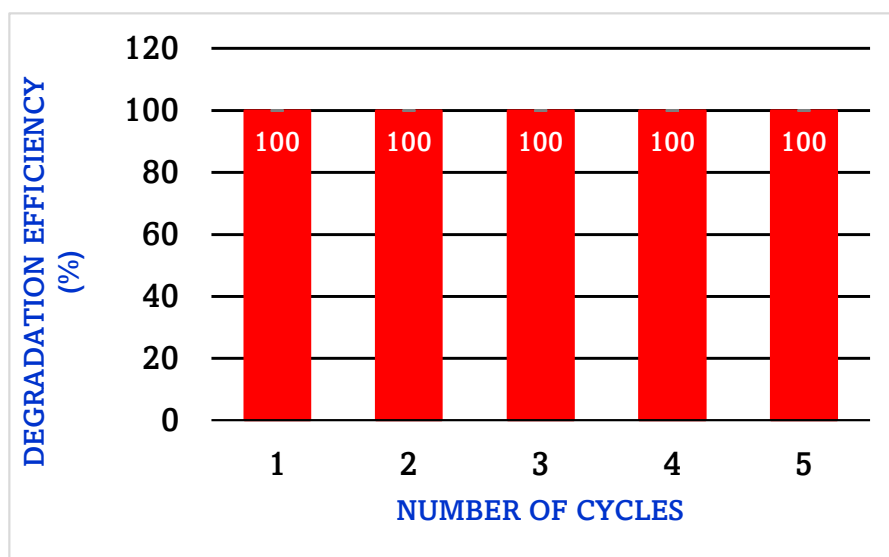


Figure 13. The degradation profile of $g\text{-C}_3\text{N}_4$ for five cycles.

The specifics of sample collection and the reusable process may vary depending on the photocatalyst being tested and the experimental protocol used. Sample collection: It is essential to collect representative samples of the photocatalyst before and after each cycle of the reusability test. The samples were collected using two distinct techniques. First, the samples were allowed to settle down after the experiment via sedimentation. After the catalyst material had settled, the photodegraded AR-26 sample in water was decanted. Second, the photocatalyst at the bottom was washed three times with distilled water, then once with methanol using a filtration technique with Whatman No: 41 filter paper. The reusable process should be designed in such a way that the photocatalyst is fully recovered and can be reused without loss of activity. The process may include washing the photocatalyst with water and methanol solvent to remove any adsorbed or reacted species, followed by drying in an oven and calcination at $350\text{ }^{\circ}\text{C}$ to regenerate the photocatalyst.

The XRD and TGA measurements were performed before and after five cycles of photocatalytic activity to provide insight into the stability of the g-C₃N₄ photocatalyst. Figure 14 compares the XRD and TGA curves before and after the photodegradation experiment and shows that the g-C₃N₄ structure was unaffected. The TGA was used to determine that no change in the thermal properties occurred before or after the experiment, and the results were positive. This is depicted in Figure 15.

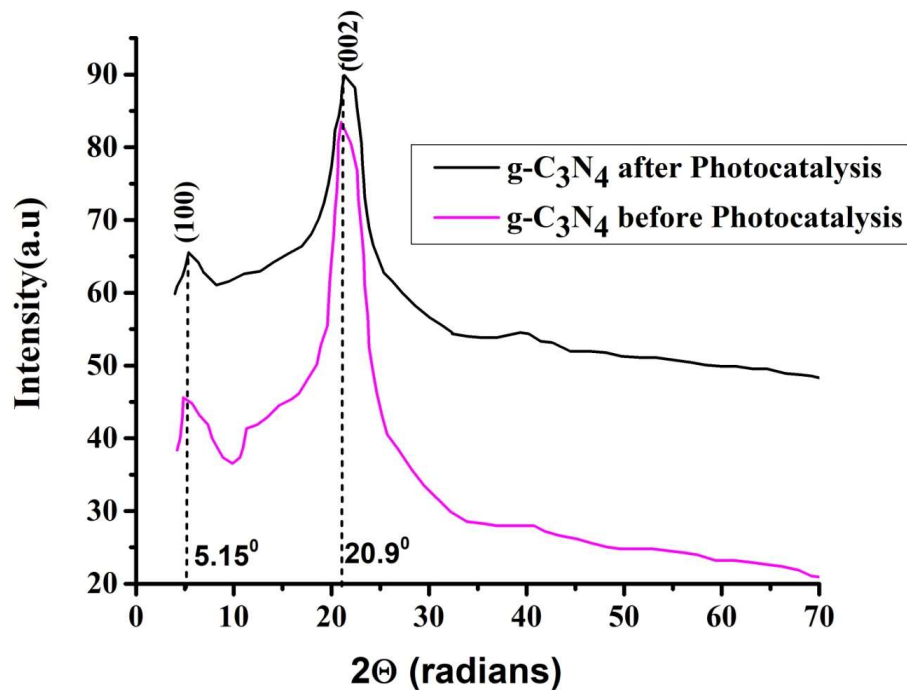


Figure 14. XRD curves of g-C₃N₄ before and after the photodegradation experiment.

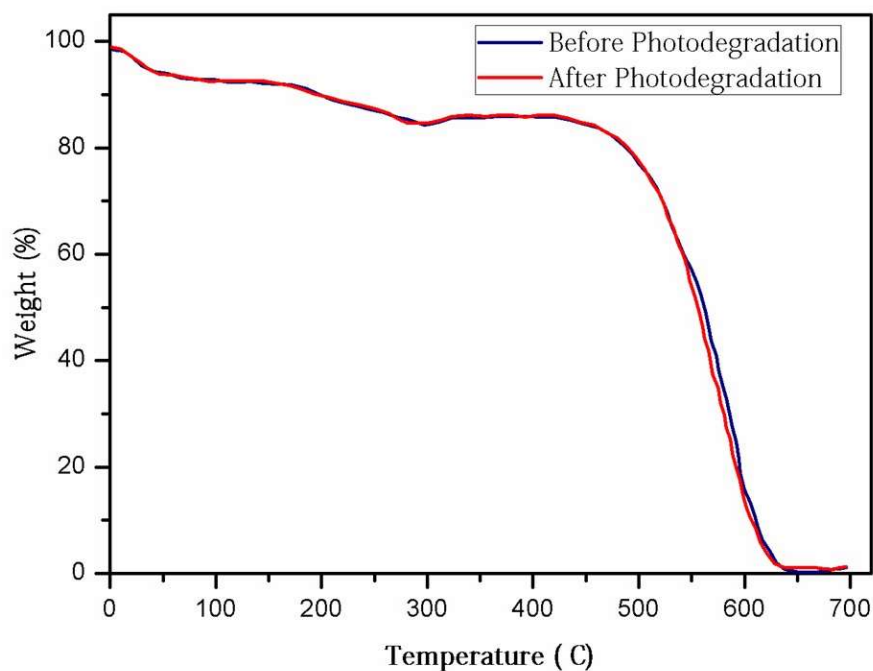


Figure 15. TGA curves of g-C₃N₄ before and after the photodegradation experiment.

4. Conclusions

The present study reports the photocatalytic breakdown of the azo dye AR-26 using UV-A irradiation and g-C₃N₄ as a photocatalyst in pure water and effluent water. Both matrices have rather high removal rates. Effluent water has a complex composition, which comprises both inorganic and organic compounds, explaining why it degrades more slowly. The scavenging tests confirmed the importance of h⁺ and O₂^{•−} in the reaction process. The photocatalytic degradation of the examined drug was discovered to comprise oxidation, dealkylation, and cleavage of the methoxy group. When pure water was employed as a media, the microalgae *Chlorococcum* sp. and *Dunaliella tertiolecta* showed no growth inhibition and hence a low toxicity from the beginning and throughout the photocatalytic process. However, when effluent water was used as a matrix, the number of reported side effects rose. However, after 180 min, the effects appeared to have disappeared. The results showed that AR-26 may be successfully eliminated using heterogeneous photocatalysis, such as g-C₃N₄ without the production of harmful IPs. As g-C₃N₄ reacts to visible light and may thus be activated by solar light, heterogeneous photocatalysis using g-C₃N₄ is viewed as a potential technique for pharmaceutical elimination after an effective separation of the photocatalyst or its immobilisation on suitable substrates.

Author Contributions: Conceptualization, S.N.M.; Methodology, M.B.P. and D.M.; Validation, S.A.A.-Z., S.N.M., A.A.O., D.M., A.K., N.S.T. and M.A.; Formal analysis, A.Y.P., A.A.O. and A.S.; Investigation, A.Y.P., D.M. and N.S.T.; Resources, A.K. and A.S.; Data curation, A.Y.P. and N.S.T.; Writing—original draft, S.A.A.-Z., M.B.P., S.N.M., N.M., V.G., A.S. and M.A.; Writing—review & editing, A.A.O., N.M. and A.K. All authors have read and agreed to the published version of the manuscript.

Funding: This research has been funded by the Scientific Research Deanship at the University of Ha'il-Saudi Arabia through project number RG-21 032.

Data Availability Statement: Not Applicable.

Acknowledgments: This research has been funded by the Scientific Research Deanship at the University of Ha'il-Saudi Arabia through project number RG-21 032. Authors thanks to the Vision Group for Science and Technology (VGST), Govt. of Karnataka, Bengaluru, India.

Conflicts of Interest: The authors here declare that there is no conflict of interest regarding the publication of this research article.

References

- Calisto, V.; Esteves, V.I. Psychiatric Pharmaceuticals in the Environment. *Chemosphere* **2009**, *77*, 1257–1274. [\[CrossRef\]](#) [\[PubMed\]](#)
- Fatta-Kassinos, D.; Meric, S.; Nikolaou, A. Pharmaceutical Residues in Environmental Waters and Wastewater: Current State of Knowledge and Future Research. *Anal. Bioanal. Chem.* **2011**, *399*, 251–275. [\[CrossRef\]](#)
- Kanakaraju, D.; Glass, B.D.; Oelgemöller, M. Titanium Dioxide Photocatalysis for Pharmaceutical Wastewater Treatment. *Environ. Chem. Lett.* **2014**, *12*, 27–47. [\[CrossRef\]](#)
- Rivera-Utrilla, J.; Sánchez-Polo, M.; Ferro-García, M.Á.; Prados-Joya, G.; Ocampo-Pérez, R. Pharmaceuticals as Emerging Contaminants and Their Removal from Water. A Review. *Chemosphere* **2013**, *93*, 1268–1287. [\[CrossRef\]](#)
- aus der Beek, T.; Weber, F.A.; Bergmann, A.; Hickmann, S.; Ebert, I.; Hein, A.; Küster, A. Pharmaceuticals in the Environment—Global Occurrences and Perspectives. *Environ. Toxicol. Chem.* **2016**, *35*, 823–835. [\[CrossRef\]](#)
- Ziarani, G.M.; Moradi, R.; Lashgari, N.; Kruger, H.G. Azo Dyes. In *Metal-Free Synthetic Organic Dyes*; Elsevier: Amsterdam, The Netherlands, 2018; Chapter 4; pp. 47–93.
- Chung, K.T. Azo dyes and human health: A review. *J. Environ. Sci. Health C Environ. Carcinog. Ecotoxicol. Rev.* **2016**, *34*, 233–261, Erratum in *J. Environ. Sci. Health C Environ. Carcinog. Ecotoxicol. Rev.* **2017**, *35*, 67. [\[CrossRef\]](#) [\[PubMed\]](#)
- Benkhaya, S.; M'rabet, S.; El Harf, A. Classifications, properties, recent synthesis and applications of azo dyes. *Heliyon* **2020**, *6*, E03271. [\[CrossRef\]](#) [\[PubMed\]](#)
- Ozturk, E.; Cinperi, N.C. Water efficiency and wastewater reduction in an integrated woolen textile mill. *J. Clean. Prod.* **2018**, *201*, 686–696. [\[CrossRef\]](#)
- Hassan, M.M.; Carr, C.M. A critical review on recent advancements of the removal of reactive dyes from dyehouse effluent by ion-exchange adsorbents. *Chemosphere* **2018**, *209*, 201–219. [\[CrossRef\]](#)
- Abe, F.R.; Soares, A.M.; de Oliveira, D.P.; Gravato, C.A. Toxicity of dyes to zebrafish at the biochemical level: Cellular energy allocation and neurotoxicity. *Environ. Pollut.* **2018**, *235*, 255–262. [\[CrossRef\]](#)

12. Du, C.F.; Xue, Y.T.; Wu, Z.S.; Wu, Z.L. Microwave-assisted one-step preparation of macadamia nut shell-based activated carbon for efficient adsorption of Reactive Blue. *New J. Chem.* **2017**, *41*, 15373–15383. [\[CrossRef\]](#)
13. Kim, S.-H.; Choi, P.-P. Enhanced Congo red dye removal from aqueous solutions using iron nanoparticles: Adsorption, kinetics, and equilibrium studies. *Dalton Trans.* **2017**, *46*, 15470–15479. [\[CrossRef\]](#)
14. Yu, B.; He, L.; Wang, Y.; Cong, H. Multifunctional PMMA@Fe₃O₄@DR Magnetic Materials for Efficient Adsorption of Dyes. *Materials* **2017**, *10*, 1239. [\[CrossRef\]](#) [\[PubMed\]](#)
15. Zhang, B.; Zhang, T.; Zhang, Z.; Xie, M. Hydrothermal synthesis of a graphene/magnetite/montmorillonite nanocomposite and its ultrasonically assisted methylene blue adsorption. *J. Mater. Sci.* **2019**, *54*, 11037–11055. [\[CrossRef\]](#)
16. González-Alfaro, Y.; Aranda, P.; Fernandes, F.; Wicklein, B.; Darder, M.; Ruiz-Hitzky, E. Multifunctional Porous Materials Through Ferrofluids. *Adv. Mater.* **2011**, *23*, 5224–5228. [\[CrossRef\]](#)
17. Darder, M.; González-Alfaro, Y.; Aranda, P.; Ruiz-Hitzky, E. Silicate-based multifunctional nanostructured materials with magnetite and Prussian blue: Application to cesium uptake. *RSC Adv.* **2014**, *4*, 35415–35421. [\[CrossRef\]](#)
18. Huang, G.; Kang, W.; Geng, Q.; Xing, B.; Liu, Q.; Jia, J.; Zhang, C. One-Step Green Hydrothermal Synthesis of Few-Layer Graphene Oxide from Humic Acid. *Nanomaterials* **2018**, *8*, 215. [\[CrossRef\]](#) [\[PubMed\]](#)
19. Singh, S.P.; Li, Y.; Zhang, J.; Tour, J.M.; Arnusch, C.J. Sulfur-Doped Laser-Induced Porous Graphene Derived from Polysulfone-Class Polymers and Membranes. *ACS Nano* **2018**, *12*, 289–297. [\[CrossRef\]](#) [\[PubMed\]](#)
20. Gómez-Carnota, D.; Barriada, J.L.; Rodríguez-Barro, P.; Sastre de Vicente, M.E.; Herrero, R. Sustainable Low-Cost Phosphorus Recovery Using Nanostructured Materials with Reusability Potential. *Nanomaterials* **2023**, *13*, 1167. [\[CrossRef\]](#)
21. Aboutaleb, W.A.; El-Salamony, R.A. Effect of Fe₂O₃-CeO₂ nanocomposite synthesis method on the Congo red dye photodegradation under visible light irradiation. *Mater. Chem. Phys.* **2019**, *236*, 121724. [\[CrossRef\]](#)
22. Patil, S.M.; Deshmukh, S.P.; More, K.V.; Shevale, V.B.; Delekar, S.D. Sulfated TiO₂/WO₃ nanocomposite: An efficient photocatalyst for degradation of Congo red and methyl red dyes under visible light irradiation. *Mater. Chem. Phys.* **2019**, *225*, 247–255. [\[CrossRef\]](#)
23. Mancuso, A.; Blangetti, N.; Sacco, O.; Freyria, F.S.; Bonelli, B.; Esposito, S.; Sannino, D.; Vaiano, V. Photocatalytic Degradation of Crystal Violet Dye under Visible Light by Fe-Doped TiO₂ Prepared by Reverse-Micelle Sol–Gel Method. *Nanomaterials* **2023**, *13*, 270. [\[CrossRef\]](#) [\[PubMed\]](#)
24. Dong, J.; Zhang, Y.; Hussain, M.I.; Zhou, W.; Chen, Y.; Wang, L.-N. g-C₃N₄: Properties, Pore Modifications, and Photocatalytic Applications. *Nanomaterials* **2022**, *12*, 121. [\[CrossRef\]](#) [\[PubMed\]](#)
25. Obregon, S.; Vazquez, A.; Ruiz-Gomez, M.A.; Rodriguez-Gonzalez, V. SBA-15 assisted preparation of mesoporous g-C₃N₄ for photocatalytic H₂ production and Au³⁺ fluorescence sensing. *Appl. Surf. Sci.* **2019**, *488*, 205–212. [\[CrossRef\]](#)
26. Ong, W.J.; Tan, L.L.; Ng, Y.H.; Yong, S.T.; Chai, S.P. Graphitic Carbon Nitride (g-C₃N₄)-Based Photocatalysts for Artificial Photosynthesis and Environmental Remediation: Are We a Step Closer to Achieving Sustainability? *Chem. Rev.* **2016**, *116*, 7159–7329. [\[CrossRef\]](#)
27. Bairamis, F.; Konstantinou, I.; Petrakis, D.; Vaimakis, T. Enhanced Performance of Electrospun Nanofibrous TiO₂/g-C₃N₄ Photocatalyst in Photocatalytic Degradation of Methylene Blue. *Catalysts* **2019**, *9*, 880. [\[CrossRef\]](#)
28. Wen, J.; Xie, J.; Chen, X.; Li, X. A Review on g-C₃N₄-Based Photocatalysts. *Appl. Surf. Sci.* **2017**, *391*, 72–123. [\[CrossRef\]](#)
29. Liu, J.; Wei, X.; Sun, W.; Guan, X.; Zheng, X.; Li, J. Fabrication of S-Scheme CdS-g-C₃N₄-Graphene Aerogel Heterojunction for Enhanced Visible Light Driven Photocatalysis. *Environ. Res.* **2021**, *197*, 111136. [\[CrossRef\]](#)
30. Liu, D.; Li, C.; Zhao, C.; Zhao, Q.; Niu, T.; Pan, L.; Xu, P.; Zhang, F.; Wu, W.; Ni, T. Facile Synthesis of Three-Dimensional Hollow Porous Carbon Doped Polymeric Carbon Nitride with Highly Efficient Photocatalytic Performance. *Chem. Eng. J.* **2022**, *438*, 135623. [\[CrossRef\]](#)
31. Liu, D.; Li, C.; Ge, J.; Zhao, C.; Zhao, Q.; Zhang, F.; Ni, T.; Wu, W. 3D Interconnected g-C₃N₄ Hybridized with 2D Ti₃C₂ MXene Nanosheets for Enhancing Visible Light Photocatalytic Hydrogen Evolution and Dye Contaminant Elimination. *Appl. Surf. Sci.* **2022**, *579*, 152180. [\[CrossRef\]](#)
32. Leelavathi, H.; Muralidharan, R.; Abirami, N.; Tamizharasan, S.; Sankeetha, S.; Kumarasamy, A.; Arulmozhi, R. Construction of Step-Scheme g-C₃N₄/Co/ZnO Heterojunction Photocatalyst for Aerobic Photocatalytic Degradation of Synthetic Wastewater. *Colloids Surf. A Physicochem. Eng. Asp.* **2023**, *656*, 130449. [\[CrossRef\]](#)
33. Bairamis, F.; Konstantinou, I. WO₃ Fibers/g-C₃N₄ Z-Scheme Heterostructure Photocatalysts for Simultaneous Oxidation/Reduction of Phenol/Cr (VI) in Aquatic Media. *Catalysts* **2021**, *11*, 792. [\[CrossRef\]](#)
34. Pei, X.; An, W.; Zhao, H.; He, H.; Fu, Y.; Shen, X. Enhancing Visible-Light Degradation Performance of g-C₃N₄ on Organic Pollutants by Constructing Heterojunctions via Combining Tubular g-C₃N₄ with Bi₂O₃ Nanosheets. *J. Alloys Compd.* **2023**, *934*, 167928. [\[CrossRef\]](#)
35. John, A.; Rajan, M.S.; Thomas, J. Carbon Nitride-Based Photocatalysts for the Mitigation of Water Pollution Engendered by Pharmaceutical Compounds. *Environ. Sci. Pollut. Res.* **2021**, *28*, 24992–25013. [\[CrossRef\]](#) [\[PubMed\]](#)
36. Go, S.; Kim, J.; Park, S.S.; Kim, M.; Lim, H.; Kim, J.-Y.; Lee, D.-W.; Im, J. Synergistic Use of Hyperspectral UV-Visible OMI and Broadband Meteorological Imager MODIS Data for a Merged Aerosol Product. *Remote Sens.* **2020**, *12*, 3987. [\[CrossRef\]](#)
37. Kim, J.; Lee, J.; Lee, H.C.; Higurashi, A.; Takemura, T.; Song, C.H. Consistency of the aerosol type classification from satellite remote sensing during the Atmospheric Brown Cloud–East Asia Regional Experiment campaign. *J. Geophys. Res. Atmos.* **2007**, *112*, D22. [\[CrossRef\]](#)

38. Torres, O.; Ahn, C.; Chen, Z. Improvements to the OMI near-UV aerosol algorithm using A-train CALIOP and AIRS observations. *Atmos. Meas. Tech.* **2013**, *6*, 3257–3270. [\[CrossRef\]](#)
39. Baxendale, J.H.; Bridge, N.K. The photoreduction of some ferric compounds in aqueous solution. *J. Phys. Chem.* **1955**, *59*, 783–788. [\[CrossRef\]](#)
40. Calvert, J.; Pitts, J.N. Liquid-Phase Chemical Actinometry Using Potassium Ferrioxalate. In *Photochemistry*; John Wiley: New York, NY, USA, 1966; pp. 783–786.
41. Spyrou, A.; Tzamaria, A.; Dormousoglou, M.; Skourti, A.; Vlastos, D.; Papadaki, M.; Antonopoulou, M. The overall assessment of simultaneous photocatalytic degradation of Cimetidine and Amisulpride by using chemical and genotoxicological approaches. *Sci. Total Environ.* **2022**, *838*, 156140. [\[CrossRef\]](#) [\[PubMed\]](#)
42. Al-Zahrani, S.A.; Patil, M.B.; Mathad, S.N.; Patil, A.Y.; Otaibi, A.A.; Masood, N.; Mansour, D.; Khan, A.; Manikandan, A.; Syafri, E. Photocatalytic Degradation of Textile Orange 16 Reactive Dye by ZnO Nanoparticles Synthesized via Green Route Using Punica Granatum Leaf Extract. *Crystals* **2023**, *13*, 172. [\[CrossRef\]](#)
43. Dai, H.; Zhang, S.; Xu, G.; Peng, Y.; Gong, L.; Li, X.; Li, Y.; Lin, Y.; Chen, G. Highly photoactive heterojunction based on g-C₃N₄ nanosheets decorated with dendritic zinc (II) phthalocyanine through axial coordination and its ultrasensitive enzyme-free sensing of choline. *RSC Adv.* **2014**, *4*, 58226–58230. [\[CrossRef\]](#)
44. Antonopoulou, M.; Hela, D.; Konstantinou, I. Photocatalytic degradation kinetics, mechanism and ecotoxicity assessment of tramadol metabolites in aqueous TiO₂ suspensions. *Sci. Total Environ.* **2016**, *545–546*, 476–485. [\[CrossRef\]](#)
45. Calza, P.; Hadjicostas, C.; Sakkas, V.A.; Sarro, M.; Minero, C.; Medana, C.; Albanis, T.A. Photocatalytic transformation of the antipsychotic drug risperidone in aqueous media on reduced graphene oxide—TiO₂ composites. *Appl. Catal. B Environ.* **2016**, *183*, 96–106. [\[CrossRef\]](#)
46. Konstas, P.S.; Kosma, C.; Konstantinou, I.; Albanis, T. Photocatalytic Treatment of Pharmaceuticals in Real Hospital Wastewaters for Effluent Quality Amelioration. *Water* **2019**, *11*, 2165. [\[CrossRef\]](#)
47. Chen, C.; Li, X.; Ma, W.; Zhao, J.; Hidaka, H.; Serpone, N. Effect of Transition Metal Ions on the TiO₂-Assisted Photodegradation of Dyes under Visible Irradiation: A Probe for the Interfacial Electron Transfer Process and Reaction Mechanism. *J. Phys. Chem. B* **2002**, *106*, 318–324. [\[CrossRef\]](#)
48. Papailias, I.; Todorova, N.; Giannakopoulou, T.; Ioannidis, N.; Boukos, N.; Athanasekou, C.P.; Dimotikali, D.; Trapalis, C. Chemical vs thermal exfoliation of g-C₃N₄ for NO_x removal under visible light irradiation. *Appl. Catal. B Environ.* **2018**, *239*, 16–26. [\[CrossRef\]](#)
49. Kobkeatthawin, T.; Chaveanghong, S.; Trakulmututa, J.; Amornsakchai, T.; Kajitvichyanukul, P.; Smith, S.M. Photocatalytic Activity of TiO₂/g-C₃N₄ Nanocomposites for Removal of Monochlorophenols from Water. *Nanomaterials* **2022**, *12*, 2852. [\[CrossRef\]](#) [\[PubMed\]](#)
50. Xu, T.; Wang, D.; Dong, L.; Shen, H.; Lu, W.; Chen, W. Graphitic carbon nitride co-modified by zinc phthalocyanine and graphene quantum dots for the efficient photocatalytic degradation of refractory contaminants. *Appl. Catal. B Environ.* **2019**, *244*, 96–106. [\[CrossRef\]](#)
51. Skibiński, R. Identification of photodegradation product of amisulpride by ultra-high-pressure liquid chromatography–DAD/ESI-quadrupole time-of-flight-mass spectrometry. *J. Pharm. Biomed. Anal.* **2011**, *56*, 904–910. [\[CrossRef\]](#)
52. Lasyal, R.; Hoel, A. Facile synthesis of IrO₂ nanoclusters and their application as catalysts in the degradation of azo dyes. *Turk. J. Chem.* **2018**, *42*, 941–957.
53. Gomes, J.F.; Lopes, A.; Gmurek, M.; Quinta-Ferreira, R.M.; Martins, R.C. Study of the influence of the matrix characteristics over the photocatalytic ozonation of parabens using Ag-TiO₂. *Sci. Total Environ.* **2019**, *646*, 1468–1477. [\[CrossRef\]](#) [\[PubMed\]](#)

Disclaimer/Publisher’s Note: The statements, opinions and data contained in all publications are solely those of the individual author(s) and contributor(s) and not of MDPI and/or the editor(s). MDPI and/or the editor(s) disclaim responsibility for any injury to people or property resulting from any ideas, methods, instructions or products referred to in the content.